MATERIALS CHEMISTRY
FRONTIERS

CHINESE CHEMICAL SOCIETY

ROYAL SOCIETY OF CHEMISTRY

RESEARCH ARTICLE

View Article Online
View Journal | View Issue

Cite this: *Mater. Chem. Front.*, 2025, **9**, 1002

Perovskite-inspired low-dimensional hybrid azetidinium bismuth halides: $[(CH_2)_3NH_2]_3Bi_2X_9$ (X = I, Br, Cl)†

Young Un Jin, *[a] Bernd Marler, [b] Andrei N. Salak, [c]
Marianela Escobar-Castillo, [a] Niels Benson [d] and Doru C. Lupascu [a]

Received 10th October 2024,
Accepted 20th January 2025

DOI: 10.1039/d4qm00878b

rsc.li/frontiers-materials

Bi-based halide perovskites have been considered as alternatives to Pb-based perovskites with the intention of avoiding the use of lead in the field of photovoltaics. Over the last few years, novel Bi-based halide perovskites have shown potential in reaching good photovoltaic performance, as suggested by their similar electronic structure to Pb-based perovskites. Nevertheless, their lower dimensionality entails poor charge carrier transport. It has been consistently stated that the role of the A-site should be further studied. To explore this proposition, we have synthesized three different Bi-based halides with substitution on the A-site by azetidinium cations. In this contribution we report fundamental observations of azetidinium bismuth halides, $[(CH_2)_3NH_2]_3Bi_2I_9$, $[(CH_2)_3NH_2]_3Bi_2Br_9$, and $[(CH_2)_3NH_2]_3Bi_2Cl_9$ with prospects in optoelectronics and photovoltaics. These new materials exhibit 0D and 2D crystal structures at a molecular level and the optical feature of an excitonic band state.

Introduction

The halide perovskite system has given rise to new developments in optoelectronics, especially in photovoltaics.[1–3] In ABX_3 halides, research has concentrated on Pb-based iodide or halide mixtures due to their radical rise in power conversion efficiency (PCE). This is due to a large absorption coefficient, low exciton binding energy, and long charge carrier diffusion length compared to other divalent metal-based halides.[4–8] Despite this, these materials are not environmentally friendly as they contain Pb as a pollutant. Thus, there has been an effort to find alternatives for the B-site. Bi^{3+} has been considered a reasonable and less toxic B-site alternative. It has a similar atomic number, ionic radius, and electronic structure to Pb^{2+}.[9–12] In general, it cannot be directly used to construct a conventional ABX_3 perovskite stoichiometry because of imbalanced charge neutrality. Therefore, Bi-based metal halides are considered perovskite-derivatives, where the chemical composition is $A_3Bi_2X_9$, which is ordered with one vacant Bi site in its unit cell.[13,14] $A_3Bi_2X_9$ can typically take two types of dimensionality: 0-dimensional (0D) or 2-dimensional (2D).[15–18] The 0D type forms $[Bi_2X_9]$-dimers that share the face of an octahedron and are isolated by an A-site, unlike the $[BX_6]$ single octahedron in the normal 3D perovskite structure. This induces a large difference in electronic properties compared to 3D perovskites, such as charge carrier mobility, effective mass, and recombination channels.[17,18] Inorganic $Cs_3Bi_2I_9$ and organic–inorganic hybrid $(MA)_3Bi_2I_9$ (where MA is methylammonium, $CH_3NH_3^+$) are 0D type. They have been applied in photovoltaics in single-junction cells. However, the PCE did not exceed 5%, due to the strong charge localisation in the dimers, the indirect nature of the bandgap, and deep defect states.[12,19–21] Nevertheless, the great stability and suitable bandgap can still prove potentially useful in photovoltaics. The 2D layered type forms octahedral networks with corner-sharing $[BiX_6]$ sites with low density, especially in the case of the small radius of the A-site cation or a large halide anion: $K_3Bi_2I_9$, $Rb_3Bi_2I_9$ and $(NH_4)_3Bi_2I_9$ adopt 2D layered systems.[22,23] These systems commonly exhibit higher conductivity than 0D-systems and a direct bandgap. Therefore, the 2D type might be more suitable than the 0D type in terms of light absorbtion.[23,24] Although the 2D-systems exhibit better preconditions for performance in solar cells, the values of the PCEs have not been reported to be as high as those for the 0D type due to deep trap states.[12,25] In addition, they have not been employed in the fabrication of a photovoltaic device to date.

---

[a] *Institute for Materials Science and Center for Nanointegration Duisburg-Essen (CENIDE), University of Duisburg-Essen, 45141 Essen, Germany. E-mail: young.jin@uni-due.de*

[b] *Institute of Geology, Mineralogy and Geophysics, Ruhr-University Bochum, 44780 Bochum, Germany*

[c] *Department of Materials and Ceramics Engineering, CICECO-Aveiro Institute of Materials, University of Aveiro, 3810-193 Aveiro, Portugal*

[d] *Institute of Technology for Nanostructures (NST), University of Duisburg-Essen, 47057 Duisburg, Germany*

† Electronic supplementary information (ESI) available. CCDC 2333115, 2333116 and 2333118. For ESI and crystallographic data in CIF or other electronic format see DOI: **https://doi.org/10.1039/d4qm00878b**

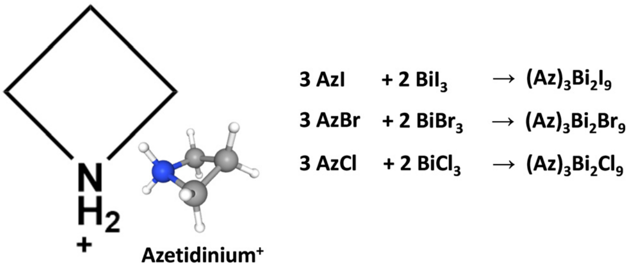

Fig. 1 Structure of the azetidinium molecular cation and chemical reactions for the synthesis of $(Az)_3Bi_2X_9$.

A-site compositional engineering for $A_3Bi_2X_9$ hybrid halides can be key to realizing optoelectronic performance, because the dipole of the organic cation at the A-site can greatly influence the electronic structure *via* a transformation in dimensionality.[26] Ünlü *et al.* made devices with replacement not only by alkali-metal cations but also by some small organic cations on the A-site. They reported photovoltaic performance with a good match to the thin-film properties of $A_3Bi_2I_9$.[27]

We have used the azetidinium cation (Az^+) on the cationic sublattice of $A_3Bi_2X_9$ (X = I, Br, Cl). Azetidinium, $[(CH_2)_3NH_2]^+$, has a suitable effective ionic radius to replace MA and FA (formamidinium, $CH(NH_2)_2{}^+$).[28,29] The molecular structure of Az^+ is heterocyclic with one nitrogen and three carbons. The carbon–nitrogen ring structure is not flat, and it is polar (Fig. 1). Az^+ has been investigated for its phase transition properties, especially in formate-based and cyanide-bridged perovskite systems.[30–32] $(Az)PbI_3$ has been synthesized and yields a PCE of 1.15% in a photovoltaic device.[33,34] Recently, our group confirmed the applicability of Az^+ incorporation into a lead-free metal halide system with the synthesis of $(Az)_2AgBiBr_6$, displaying 1D chains of octahedra in the crystal lattice.[35]

In this paper, we chose $(Az)_3Bi_2X_9$ (X = I, Br, Cl) for a detailed analysis, attempting to expand the range of potential absorber materials.

Experimental

Synthesis

Single crystals of $(Az)_3Bi_2X_9$ can be grown, but this is a time-intensive process, and we have not been able in all cases to produce single crystals which were large enough, not twinned, and not intergrown with other crystals. We thus chose to use polycrystalline samples for structural studies.

Polycrystalline $(Az)_3Bi_2X_9$ powders were synthesized by an evaporation method. A brief depiction of the chemical reaction for the synthesis of azetidinium bismuth halide is presented in Fig. 1. We used bismuth(III) iodide (99%) (BiI_3), bismuth(III) bromide (>98%) ($BiBr_3$) from Sigma-Aldrich, and bismuth(III) chloride (99.999%) ($BiCl_3$) from ACROS Organics. Azetidinium chloride (97%) (AzCl) was purchased from Sigma-Aldrich. Azetidinium bromide (AzBr) was synthesized in our laboratory by the reaction of hydrobromic acid (48%) (HBr) and azetidine (98%, Thermo Fisher Scientific). Azetidinium iodide (AzI) was synthesized by the reaction of hydroiodic acid (55–58%) (HI) and azetidine (98%). Powdered $(Az)_3Bi_2I_9$ was synthesized by the evaporation of a 0.2 M precursor at 65 °C, which consisted of AzI and BiI_3 dissolved in *N*,*N*-dimethylformamide. The polycrystalline powder of $(Az)_3Bi_2Br_9$ was synthesized by evaporation of a precursor made from AzBr and $BiBr_3$ dissolved in acetonitrile at 80 °C in a vacuum oven. The polycrystalline powder of $(Az)_3Bi_2Cl_9$ was synthesized by evaporation of a 0.3 M precursor containing AzCl and $BiCl_3$ dissolved in γ-butyrolactone. The precursor solution was filtered through a PTFE (polytetrafluorethylene) membrane filter of 0.45 μm pore size. The acquired crystals of $(Az)_3Bi_2Cl_9$ were crushed, and then cleaned in isopropanol.

Crystal structure

The crystal structures of the $(Az)_3Bi_2X_9$ materials were determined from powder X-ray diffraction (PXRD) data by the direct method using the program EXPO 2014.[36] It was an intricate matter to obtain the underlying crystal structure model from the powder diffraction data. The results are given in Fig. 2. Subsequently, the structural models were refined using the Rietveld method. The refinements converged to convincing chi^2 and *R*-values (see Table 1) confirming the correctness of the structural models. All materials could be obtained as single phases in specific synthesis runs and always as polycrystalline powders. In the case of $(Az)_3Bi_2I_9$, the structure was refined from the dataset of a sample that contained an additional, silver-containing, impurity phase (approx. 10%). The structure of $(Az)_3Bi_2Cl_9$ was refined from the dataset of a sample that contained a small amount of BiOCl (refined: 1.4%). The crystals in the latter two samples showed a much higher degree of structural order than the crystals of the corresponding monophasic samples.

For further details, please see the ESI.†

Results and discussion

$(Az)_3Bi_2I_9$ exhibits hexagonal symmetry, with space group $P6_3mc$ (No. 186). The crystal structure contains 4 trivalent Bi^{3+} cations and 18 I^- anions per unit cell, forming four $[BiI_6]$ octahedra. Two of these octahedra always share common faces, thereby generating two $[Bi_2I_9]$ dimers (Fig. 2). The Az^+ cations occupy specific positions surrounding the $[Bi_2I_9]$ dimers per unit cell. As the octahedra are isolated within the unit cell, they form an effectively 0D octahedral structure. The space group for $(Az)_3Bi_2I_9$ is the same as those for $(MA)_3Bi_2I_9$ and $(GA)_3Bi_2I_9$. Methylammonium (MA) and guanidinium (GA) have similar effective ionic radii to Az^+.[37,38] It is expected that its structural and electrical properties will be close. In the crystal lattice, Az^+ cations have a largely random orientation with no specific location for the N atom. We assume that Az^+ is dynamically disordered at room temperature. This is the result of XRD. However, it should be considered that it is quite difficult to

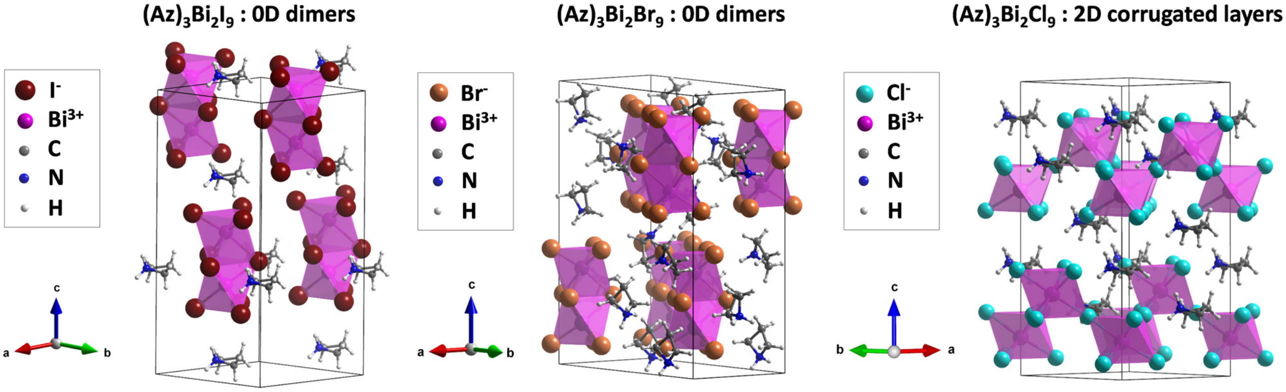

Fig. 2 Refined crystal structure diagrams of $(Az)_3Bi_2X_9$ (X = I, Br, Cl). The azetidinium cations have specific sites in the crystal lattice of $(Az)_3Bi_2X_9$ but a random orientation of the ring. The orientations of the azetidinium ring do not coincide with Rietveld refinement results but represent a snapshot of the disordered cation. (Edited by VESTA software.).

Table 1 Crystallographic parameters for the structural refinements of $(Az)_3Bi_2X_9$

Unit cell content	$C_{18}H_{48}N_6Bi_4I_{18}$	$C_{36}H_{96}N_{12}Bi_8Br_{36}$	$C_{18}H_{48}N_6Bi_4Cl_{18}$
Diffractometer	STOE STADI MP with Mythen 1 K position sensitive detector	PANalytical X'pert PRO with PIXcel3D-Medipix3 1D scanning line detector	
Wavelength	1.54059 Å (Cu Kα_1 Radiation)	1.5418 Å (Cu K$\alpha_{1/2}$ Radiation)	
Sample holder	Flat zero scattering foil	Flat Si circular plate	
2θ range of data used [°]	6.0–86.9	7. 0–94.9	7. 0–95.0
Step size [°2θ]	0.01500	0.01313	0.01313
No. contributing reflections	301	929	944
No. geometric restraints	6	26	20
No. structural parameters	23	54	39
No. profile parameters	8	15	16
FWHM at *ca.* 25°2θ [°2θ]	0.08–0.09	0.12–0.13	0.06–0.07
R_F	0.034	0.046	0.048
R_{wp}	0.110	0.130	0.136
$\chi 2$	1.83	2.19	2.31
Space group	$P6_3mc$ (No. 186)	$Cmc2_1$ (No. 36)	$P31c$ (No. 159)
Crystal lattice	Hexagonal	Orthorhombic	Trigonal
a [Å]	9.1537(1)	8.4576(3)	8.4764(1)
b [Å]	9.1537(1)	16.2886(6)	8.4764(1)
c [Å]	22.2111(4)	20.8689(5)	20.5819(5)
V_{UC} [Å^3]	1611.73(4)	2874.94(8)	1280.69(4)
Density (calc.) [g cm^{-3}]	3.574	3.035	2.363

locate C and N atoms in the vicinity of heavy scatterers like I and Bi, from XRD powder diffraction data.

$(Az)_3Bi_2Br_9$ adopts an orthorhombic lattice with the space group, $Cmc2_1$ (No. 36), which also contains 0D isolated $[Bi_2Br_9]$ dimers surrounded by Az^+ cations that are highly disordered with respect to the carbon and nitrogen positions. The structure of $(Az)_3Bi_2Br_9$ is pseudo-hexagonal and very similar to that of $(Az)_3Bi_2I_9$, but the actual symmetry is lower than that of $(Az)_3Bi_2I_9$.

$(Az)_3Bi_2Cl_9$ is distinctive, as it has a low-density 2D structure with corner-sharing $[BiCl_6]$ interconnecting octahedra. Az^+ is also highly disordered and intercalated between $[Bi_2Cl_9]$ layers. It assumes space group $P31c$ (No. 159) with trigonal symmetry. The corner-sharing only corresponds to 3 Cl^- anions in a one-octahedron framework, in which the vacant site between the $[BiCl_6]$ octahedra is occupied by disordered Az^+ cations.

The polycrystalline powder of $(Az)_3Bi_2I_9$ has a red colour (Fig. 3). The most intensive reflection is the (101) plane at 2θ = 11.77° that was confirmed by its PXRD pattern. The largest *d*-spacing in the lattice is in the (002) plane at 2θ = 7.97°, followed by (100), (101) and (102). Every reflection has a relatively large full-width-at-half-maximum (FWHM) in its PXRD pattern; thus, comparatively large strains exist in the crystal lattice. The refined polycrystalline powder of $(Az)_3Bi_2Br_9$ is yellow. The PXRD of $(Az)_3Bi_2Br_9$ has a main reflection of the (111) plane at 2θ = 12.56°, which is not identical to $(Az)_3Bi_2I_9$ owing to its different crystal symmetry. $(Az)_3Bi_2Cl_9$ is an almost white powder. It generally appeared in quite highly crystalline form for every sample we synthesized, with much higher intensity values than $(Az)_3Bi_2I_9$. The (102) reflection at 2θ = 14.76° has the highest peak intensity. Its better degree of crystallinity may be due to the 2D $[BiCl_6]$ octahedral network being more rigid than isolated dimers.

Thin films

To investigate the thin-film properties, we deposited $(Az)_3Bi_2X_9$ thin-film layers with one-step spin coating as an initial step.

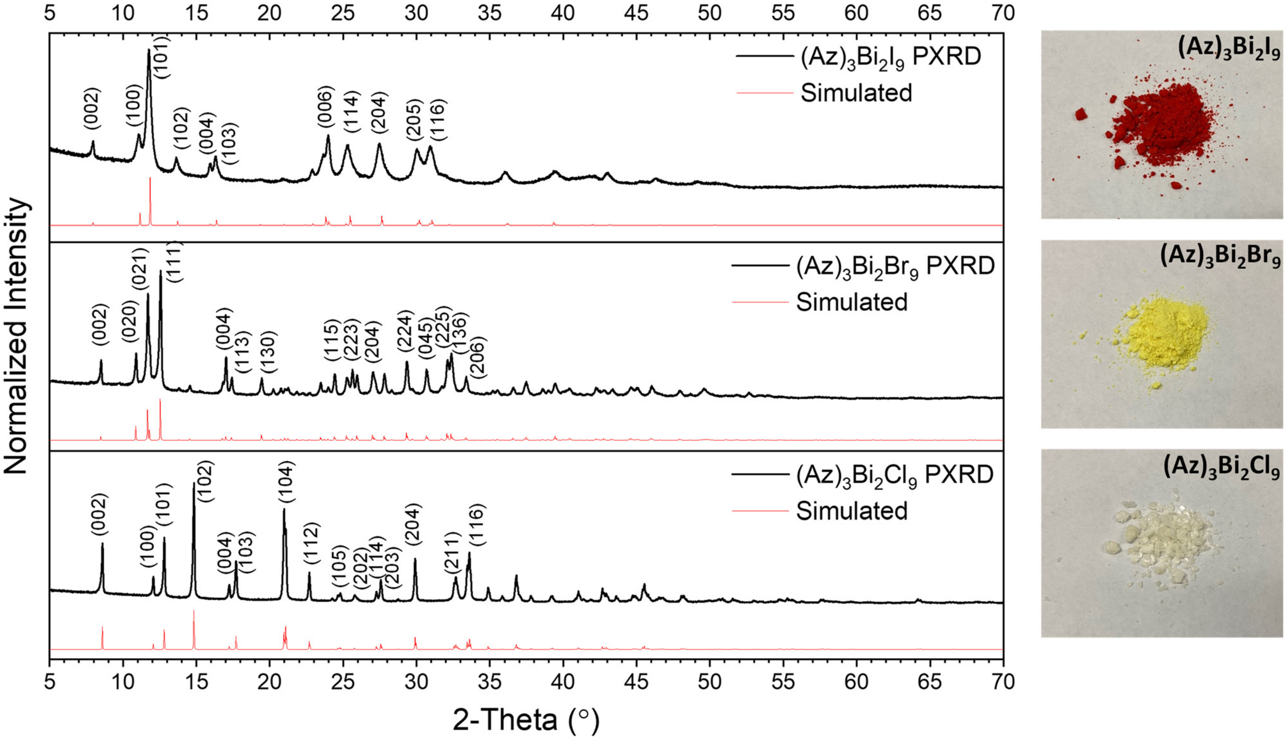

Fig. 3 Powder X-ray diffraction patterns (PXRD) of $(Az)_3Bi_2X_9$ phases with approximately randomly oriented crystals and photographs of the powdered materials. Simulated patterns based on the refined structures are shown for comparison.

According to their XRD patterns all $(Az)_3Bi_2X_9$ strongly exhibit specific grain growth. To determine the features of substrate-dependent growth, we prepared three different (transparent) substrates and coated the thin films onto those: purified normal glass, fluorine-doped tin oxide (FTO), and indium tin oxide (ITO). On a glass substrate, the thin films of $(Az)_3Bi_2I_9$ and $(Az)_3Bi_2Br_9$ show a preference for (00*l*) growth orientation with large intensities of (002), (004), and (006). $(Az)_3Bi_2Cl_9$ presented growth with (002) and (004) reflections (Fig. 4a). In the case of $(Az)_3Bi_2I_9$, the greatest intensity is the (006) reflection at $2\theta = 24.39°$, well exceeding the intensities of the (002) and (004) reflections at $2\theta = 8.15°$ and $16.24°$, respectively. (0010), and (0012) reflections with relatively small intensity at $2\theta = 41.12°$ and $49.84°$, respectively, were also detected. The diffraction pattern of $(Az)_3Bi_2Br_9$ on glass had the greatest intensity for the (002) reflection at $2\theta = 8.60°$ followed by (004) at $2\theta = 17.12°$ and then (006) at $2\theta = 25.75°$. There were lower but distinctive reflections of (0010) at $2\theta = 43.51°$ and (0012) at $2\theta = 52.81°$. At (006), (0010), and (0012) reflections peak splitting was detected. In the diffraction pattern of $(Az)_3Bi_2Cl_9$ on glass, we confirmed that the intensities of the reflections of (002) at $2\theta = 8.65°$ and (004) at $2\theta = 17.30°$ are extremely high compared to the corresponding peaks of $(Az)_3Bi_2I_9$ and $(Az)_3Bi_2Br_9$. Remarkable peak splitting happens for the (004) reflection.

Compared to the film coated on glass, the XRD pattern of $(Az)_3Bi_2I_9$ thin film on FTO shows no growth preference, so the pattern is close to its PXRD (Fig. S3, ESI†). The FTO substrate has a tetragonal structure (rutile), inducing a significant mismatch with the crystal growth of $(Az)_3Bi_2I_9$. The $(Az)_3Bi_2I_9$ thin film on ITO is similar to that on glass, but the (002) reflection is as dominant as the (006) reflection. The XRD pattern of $(Az)_3Bi_2Br_9$ on FTO presents only some very low peaks at around $2\theta = 12.5°$ and $17.5°$, corresponding to a secondary, nearly amorphous phase and some reflections of FTO, but no reflection that indicates the occurrence of $(Az)_3Bi_2Br_9$ crystals. We assume that the orthorhombic structure of $(Az)_3Bi_2Br_9$ yields an intermediate mismatch, generating increased disorder in the thin film, seen as an amorphous phase. The XRD pattern of $(Az)_3Bi_2Br_9$ on ITO presents the same pattern as on glass. Although the intensities of the reflections are much lower than those on glass. Similarly, in the XRD patterns of $(Az)_3Bi_2Cl_9$ on FTO and ITO, it was confirmed that the intensities of the (002) and (004) reflections are much lower than those on glass, although those peaks are sharp. Unlike the $(Az)_3Bi_2I_9$ and $(Az)_3Bi_2Br_9$ thin films on FTO, $(Az)_3Bi_2Cl_9$ on FTO resulted in highly textured growth because there is a lattice match with the substrate. The identification of other peaks of $(Az)_3Bi_2Cl_9$ was not simple due to the relatively high and sharp intensity of its (002) and (004) reflections. We focused on the very low-intensity region of the XRD pattern of $(Az)_3Bi_2Cl_9$ on every substrate (Fig. S3d, ESI†). The resulting patterns seemingly presented not only (00*l*) reflections but also small broad peaks, coinciding with (100), (200), and (300) orientations in all patterns.

The morphology of the $(Az)_3Bi_2X_9$ thin film was visualized in SEM images for comparison with the XRD results (Fig. 4b). The grains of $(Az)_3Bi_2I_9$ on glass are mostly platelets, which are not

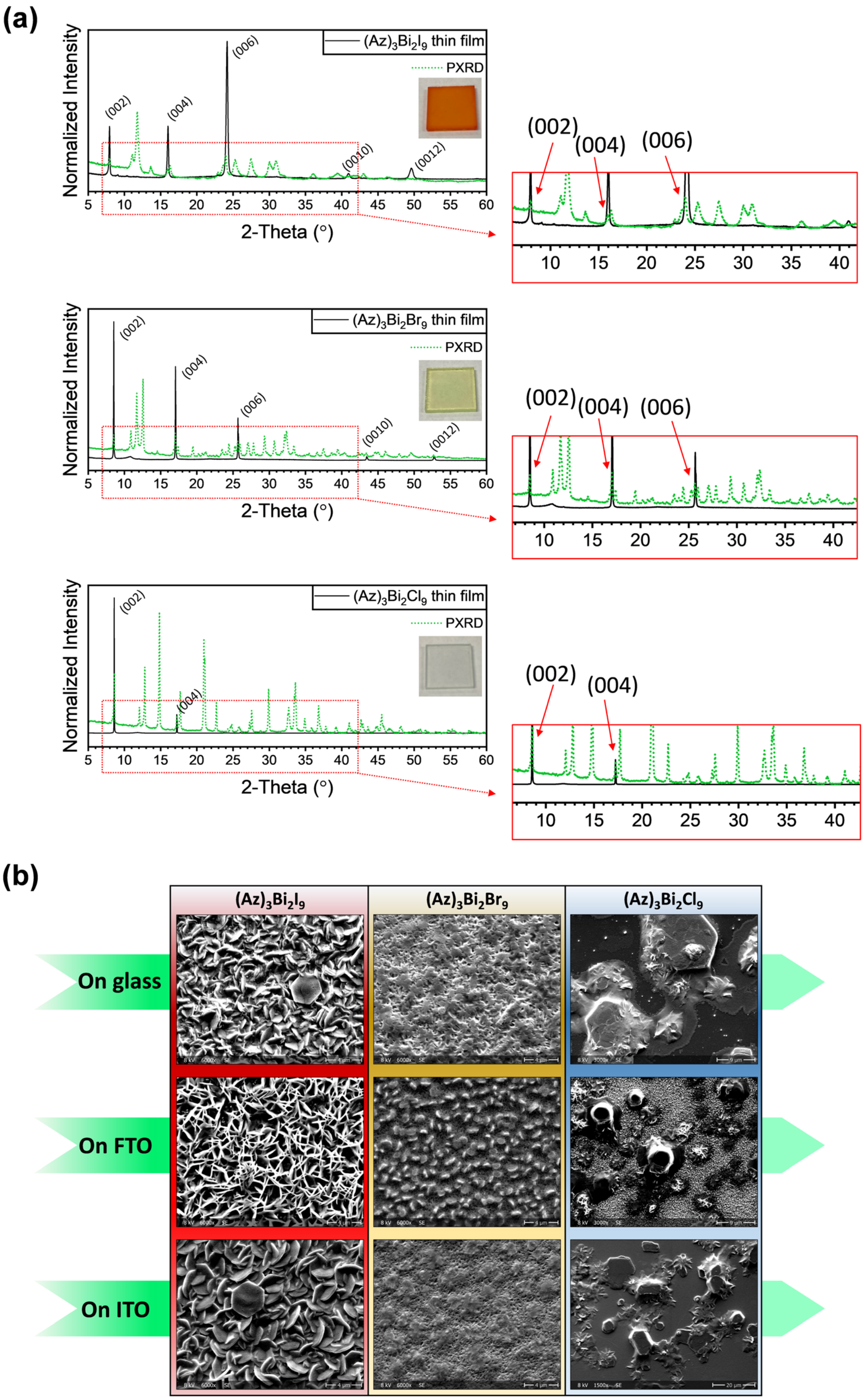

Fig. 4 (a) X-ray diffraction patterns of $(Az)_3Bi_2X_9$ thin films on glass substrate with pictures of the samples (the green dotted line represents the powder X-ray diffraction), (b) SEM morphological images of $(Az)_3Bi_2X_9$ on different transparent substrates.

coplanar with the substrate. This generates a very rough film. The morphology of $(Az)_3Bi_2I_9$ on FTO is different from that of the film on glass. A homogenous distribution of needle-like grains is displayed, but no hexagonal platelets. $(Az)_3Bi_2I_9$ on ITO has nearly the same morphology as on glass. As with its XRD pattern, the preferred (000*l*) orientation is dominant. $(Az)_3Bi_2Br_9$ on glass is less rough. The crystallites seem to have grown in star-like patterns, which have merged to form a film.

The morphological state of $(Az)_3Bi_2Br_9$ on ITO is nearly identical to that of $(Az)_3Bi_2Br_9$ coated on glass. $(Az)_3Bi_2Br_9$ on FTO has smaller grains. It seems that the crystals hardly grow, with only a low density of coverage. In addition, the shape of the grains is completely different from those on glass or ITO. The XRD pattern differs for the reflections with low intensity in Fig S3 (ESI†). $(Az)_3Bi_2Cl_9$ on glass has large hexagonal grains with small lumps that seem to be in an intermediate stage of crystal growth (Fig. 4b). However, the crystal layer does not completely cover the glass surface. This phenomenon is also shown in the films coated on FTO and ITO. The size of the grains of $(Az)_3Bi_2Cl_9$ is usually larger than those of $(Az)_3Bi_2I_9$ or $(Az)_3Bi_2Br_9$. The XRD pattern shows that the texture of the large grains corresponds to the (00*l*) reflection.

Chemical characterization

Azetidinium cations were characterized using Fourier transform infrared (FT-IR) transmittance spectra of powder samples at room temperature (Fig. 5a). The results exhibit the assignment of transmission peaks of the azetidinium cation in the crystal lattice.[34,39–41] The broad band at around 3359 cm^{-1} is considered to be the N–H stretching vibrational mode of the Az^+.[40] This band is clear in the spectrum of $(Az)_3Bi_2I_9$, but the intensity is lower in the spectra of $(Az)_3Bi_2Br_9$ and $(Az)_3Bi_2Cl_9$. This might be due to weak hydrogen bonds in these two compounds. $C_2–N^+–H_2$ stretching can be assigned to 3190–3150 cm^{-1} and $C_2–N^+–H_2$ deformations can be assigned to 1570–1530 cm^{-1} and 1445–1430 cm^{-1}.[41] The two transmission peaks of all materials at 3090–3080 cm^{-1} and 2990–2960 cm^{-1} can indicate $–CH_2$ asymmetric/symmetric stretching.[40,41] An obvious peak at 690–670 cm^{-1} is detected in all materials, which indicates azetidine ring deformation, according to the calculations and data of H. Nielsen and N. Gajhede [1989].[40]

We performed Raman spectroscopy for both powder and thin films (on glass) using a 532 nm laser from 4000 cm^{-1} to 100 cm^{-1} at room temperature (Fig. 5b). A common characteristic is observed where there are obvious Raman peaks only below 400 cm^{-1}. These Raman bands clearly indicate the

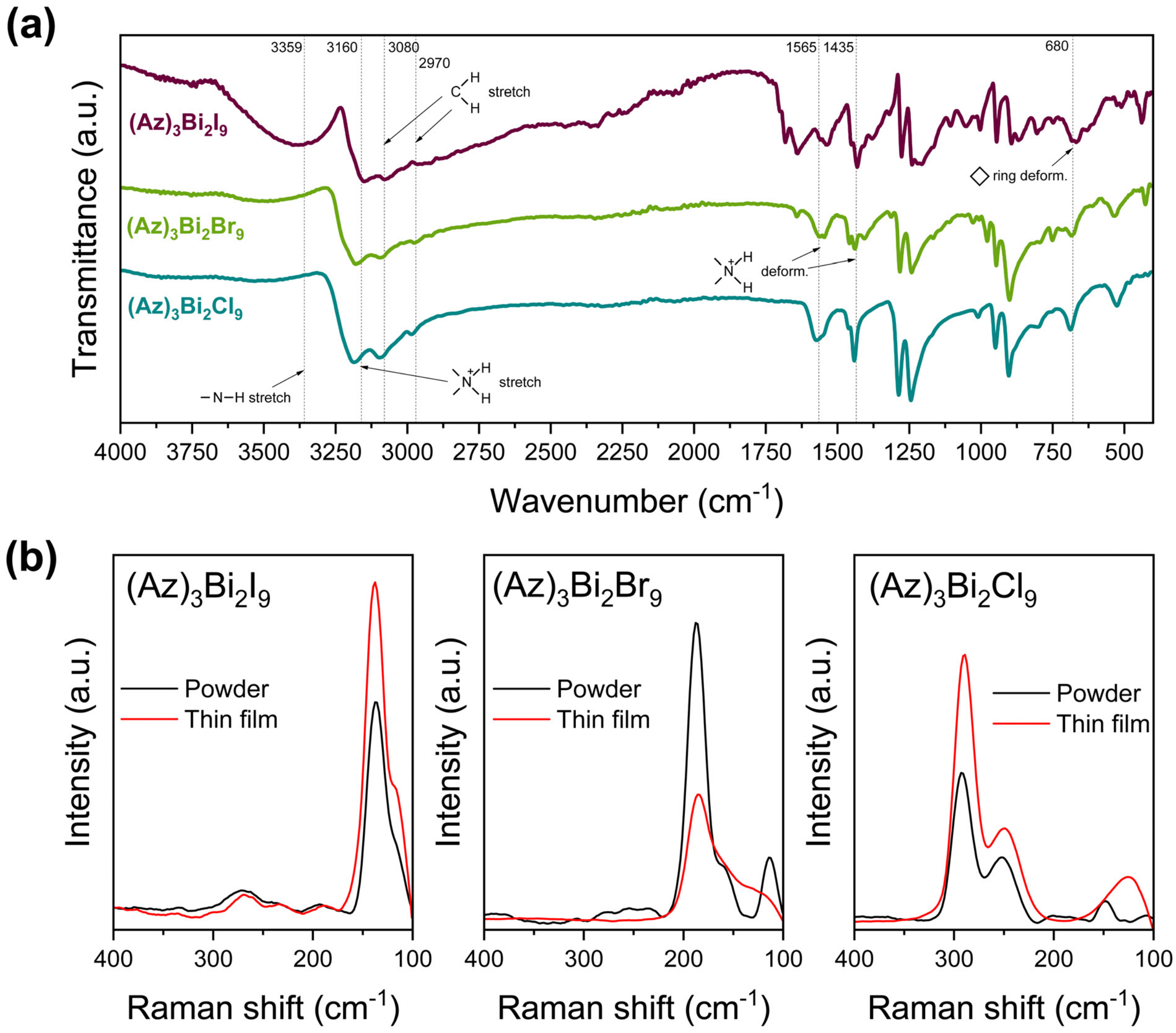

Fig. 5 (a) FT-IR spectra of $(Az)_3Bi_2X_9$ powders and (b) Raman spectra of $(Az)_3Bi_2X_9$ powders and thin films on glass (laser used: 532 nm).

vibrational mode of the $[BiX_6]^{3-}$ octahedra, in good agreement with compounds reported in the literature.[42–46]

The Raman spectrum of $(Az)_3Bi_2I_9$ powder can be explained with 2 peaks: a low-intensity one at ~118 cm^{-1} caused by the vibrational mode of a $[BiI_6]^{3-}$ singular octahedron in the $[Bi_2I_9]^{3-}$ dimers, and a high-intensity one at ~137 cm^{-1} caused by the Bi–I bonds of the internal $[BiI_6]^{3-}$ octahedron.[42,43] The spectrum of the $(Az)_3Bi_2I_9$ thin film has the same characteristics as that of the powder. The Raman spectrum of $(Az)_3Bi_2Br_9$ powder presents 3 peaks. There is a strong peak at ~187 cm^{-1} and a weaker one at ~160 cm^{-1} assigned to the Bi–Br stretching vibrational mode of the $[BiBr_6]^{3-}$ octahedron.[44] The other separate band at ~114 cm^{-1} can be assigned to the axial stretching vibrational mode of the Br–Bi–Br bridge in the $[BiBr_6]^{3-}$ octahedron.[44] The spectrum of the thin film has a weaker and unclear band compared to that of the powder. This might be because the optimized film is quite thin, leading to less Raman scattering.

In the case of the Raman spectrum of $(Az)_3Bi_2Cl_9$, the two large bands at ~293 cm^{-1} and at ~253 cm^{-1} can be assigned to Bi–Cl stretching, and the other small band at ~149 cm^{-1} can be assigned to δ (Cl–Bi–Cl) bending vibrational modes in the anionic crystal sub-lattice $[BiCl_6]^{3-}$.[45,46] A slight shift is observed in the Bi–Cl stretching bands (around 2 cm^{-1}) in the spectrum of the thin film, but the δ (Cl–Bi–Cl) bending band is shifted a long way to ~126 cm^{-1}. As we suggested above, our thin film of $(Az)_3Bi_2Cl_9$ is in an unusual state, which does not give complete coverage, while its crystallinity is very high. This factor might have a great influence on the Raman shift of the thin-film state.

Optical properties

The Tauc plot method with Kubelka–Munk transformation of diffuse optical reflectance spectra was used, extending up to 4 eV.[47,48] (Fig. 6a and b). $(F(R)h\nu)^{1/2}$ is plotted against photon energy $h\nu$, reflecting a potential indirect band transition; see Fig. 6a. By linear extrapolation, an indirect bandgap transition of $(Az)_3Bi_2I_9$ is approximately assessed as 1.97 eV; however, it seems that sub-band transitions occur at 2.52, 2.99, and 3.32 eV, although these band states are not clear in the graph. In the case of $(Az)_3Bi_2Br_9$, the dominant band transition is estimated as 2.58 eV and that of $(Az)_3Bi_2Cl_9$ is estimated as 3.12 eV in the indirect band transition plot. Noteworthy is the weak broad-band state at $(Az)_3Bi_2Cl_9$ below its dominant band transition. For comparison, $(F(R)h\nu)^2$ is also plotted against photon energy $h\nu$, where it presents a direct band transition in Fig. 6b. A direct band transition value of $(Az)_3Bi_2I_9$ is assessed as 2.09 eV, and it presents a sub-band transition at 2.51 eV followed by 2.99, and 3.35 eV, similar to its indirect band transition plot. Absorption edges in the direct band transition plots of $(Az)_3Bi_2Br_9$ and $(Az)_3Bi_2Cl_9$ are extracted as 2.67, and 3.17 eV, respectively. Additionally, $(Az)_3Bi_2Br_9$ presents a second band transition at 3.65 eV in the higher region of the band edge, which is not estimated in its indirect band transition plot.

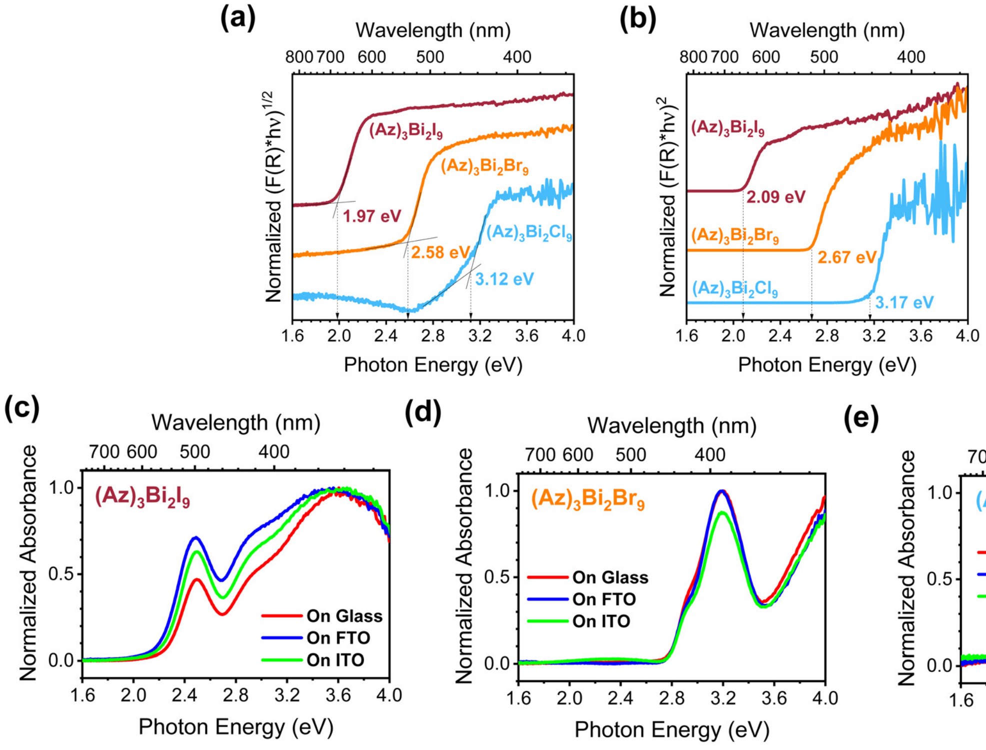

Fig. 6 Tauc plots of the polycrystalline powders of $(Az)_3Bi_2X_9$ through Kubelka–Munk transformation and bandgap estimation with (a) an indirect transition that describes photon energy *vs.* $(F(R)h\nu)^{1/2}$ and (b) a direct transition that describes photon energy *vs.* $(F(R)h\nu)^2$, and absorbance spectra of (c) $(Az)_3Bi_2I_9$, (d) $(Az)_3Bi_2Br_9$, and (e) $(Az)_3Bi_2Cl_9$ in accordance with different substrates (glass, FTO, and ITO).

For $(Az)_3Bi_2Cl_9$, the sub-band states are unclear, but the broadband state is not observed below its band edge.

For clarification of the bandgap study, absorption spectra of thin films of $(Az)_3Bi_2X_9$ on variable substrates (glass, FTO, and ITO) were measured using UV-vis spectroscopy as a subsequent step (Fig. 6c–e). Overall, the absorption spectra of the thin films present a slightly wider bandgap compared to those of the powders. There are a variety of factors for the band-shift between powders and thin films. This sort of deviation was often observed in Bi-based halides.[49] For example, for thin-film deposition of the analogue $(MA)_3Bi_2I_9$, large deviations of the bandgap appear for different fabrication methods, where the bandgap ranges from 1.8 eV to 2.2 eV.[50–52]

The absorption spectrum of the $(Az)_3Bi_2I_9$ thin film presents a steep dominant peak centered at 2.49 eV, a wide absorption band, and sub-band transitions at 3.11 eV, and 3.61 eV (Fig. 6c). This spectral structure shows similarities to those of $Cs_3Bi_2I_9$ and $(MA)_3Bi_2I_9$.[53,54] As those analogues have the same dimensionality as our $(Az)_3Bi_2I_9$, the dominant peak at 2.49 eV is assumed to be an excitonic band state. In the case of the electronic structure of $(MA)_3Bi_2I_9$, it is considered to consist of electron transitions from the ground $^1S_0$ state to the triplet excited states $^3P_2$, $^3P_1$, and $^3P_0$ of Bi^{3+} in the $[Bi_2I_9]$ dimers.[54] Therefore, it can be assumed that the sub-band transitions of $(Az)_3Bi_2I_9$ are induced in the $[Bi_2I_9]$ electron transitions. Recently, Klein *et al.* suggested that the shape of the absorption edge changes when the Tauc plot is used if the absorption edge is dominated by an excitonic transition, so the Tauc plot cannot be fitted.[55] To clarify the excitonic region, we fitted the absorbance of its thin film on glass with a Gaussian function, giving an FWHM of 285 meV and an absorption peak at 2.502 eV (Fig. S4, ESI†). The fitting of the graph shows that the dominant absorption at the band edge is an excitonic band state. It is considered that this excitonic band is caused by the localization of exciton transitions due to the electronic structure of isolated $[Bi_2I_9]$ dimers. Depending on substrates, no evident shifts of the absorption band edge were detected; only the increase in absolute absorption was presented. Compared to the thin film on glass, the excitonic absorption peaks for the thin films on ITO and on FTO are intense. The crystallinity of the thin film on ITO might tend to be lower according to our XRD dataset, but this would not be the sole factor determining an increase in the absolute value of absorption. There is no observation of preferred growth for the thin film on FTO, as shown in Fig S3 (ESI†). This indicates that the texture of the thin film decreases the dominant excitonic absorption peak of $(Az)_3Bi_2I_9$.

The absorption spectrum of $(Az)_3Bi_2Br_9$ thin film presents a strong and broad absorption centered at around 3.20 eV (Fig. 6d). This strong band can be estimated as an exciton transition, as our structural determination of $(Az)_3Bi_2Br_9$ adopts an 0D face-sharing octahedral structure like $(Az)_3Bi_2I_9$, predicting that it will have a similar electronic structure. However, it features a sub-gap observed at 2.90 eV that is partially overlapped at the exciton transition. This sub-gap is weakly distinctive; therefore, it is difficult to estimate whether it is due to an excitonic transition or a deep trap-state. Due to this sub-gap, it was difficult to ascertain the fitting of the plot for the excitonic peak with either Lorentzian or Gaussian functions. In addition, this sub-gap is not observed in the Tauc plot of the powder reflectance. The sequential band is detected at around 3.59 eV. The thin film on ITO appears to show relatively weak excitonic absorption compared to those on glass or FTO, but not that critical shift. We confirmed that the excitonic peak at around 3.19 eV of the thin film on FTO is slightly different from the others.

In the case of the thin film of $(Az)_3Bi_2Cl_9$, the absorption spectrum presents a dominant band edge at 3.35 eV followed by a sequential band at 3.52 eV (Fig. 6e). The excitonic peak near the band edge is not as obvious as those of $(Az)_3Bi_2I_9$ or $(Az)_3Bi_2Br_9$. This is considered to be due to an expansion of dimensionality in comparison with $(Az)_3Bi_2I_9$ and $(Az)_3Bi_2Br_9$, resulting in weakened excitonic confinement.[24] The thin films of $(Az)_3Bi_2Cl_9$ on glass and FTO show characteristics of linearly increasing absorption up to 3.30 eV, but that on ITO has a weak and broad absorption band up to 3.28 eV. As mentioned above, the thin film of $(Az)_3Bi_2Cl_9$ does not completely cover the substrates, regardless of the kind of substrate; therefore, it should be normal to have different defect states from $(Az)_3Bi_2I_9$ and $(Az)_3Bi_2Br_9$. In other words, this weak and broad absorption is expected to come from a deep defect state induced by the very low density of the thin-film layer. Therefore, further research into trap states or emission spectroscopy should be conducted. Meanwhile, weakening of the excitonic peak is observed with a thin film of $(Az)_3Bi_2Cl_9$ on glass compared with that on FTO. Observing that the grain size of the thin film on glass is larger than that on FTO, we assume that this is a typical phenomenon caused by its high crystallinity, resulting in a large distribution of 2-dimensional grains. The absorption spectrum of the thin film on ITO largely presents a weakened excitonic peak. Moreover, the sub-band at 3.52 eV is not distinctive. This should be re-assessed after optimization with completely filled layers.

The remarkable thing is that the excitonic peak does not exist in the powder reflectance spectra, while it is clearly visible in the thin-film absorbance spectra. There could be multiple reasons for this. One obvious option is that surface defects act as quenching sites for the excitons on the large powder surface.[56–58] Crystallite formation in powders may also include more point defects than films, but the underlying mechanisms are too complex to be resolved here.

Conclusions

It has been proven that $(Az)_3Bi_2X_9$, where the Az^+ cation is incorporated into the A-site of Bi-based halides, represent specific low-dimensional perovskite-derivatives. $(Az)_3Bi_2I_9$ and $(Az)_3Bi_2Br_9$ adopt an 0D-isolated octahedral structure, while $(Az)_3Bi_2Cl_9$ adopts a 2D corrugated layered octahedral structure at the molecular level with randomly oriented Az^+ cations in the crystal lattice. $(Az)_3Bi_2I_9$ is in a different space group to $(Az)_3Bi_2Br_9$. Due to the peculiar molecular structure and random orientation of the Az^+ cation, there is further interest in studying these systems at low temperature to determine their molecular dynamics.

The success of the synthesis of the polycrystalline powders and thin films implies that they are potential materials for optoelectronics and photovoltaics as new light absorbers. In particular, it will be worth trying to do deep research on their optical features in relation to their electronic structure. The excitonic peak that was detected in the absorbance of the thin films is not clear in the Tauc plot from the reflectance spectra of the powders. We did not identify whether they have an obviously direct or indirect transition at the forbidden band. This should be further characterized through various theoretical and experimental methods. Accordingly, we believe that this study can provide insight into developing the scientific scope for light absorbing materials in the future.

Author contributions

Y. U. J. organized the research and the experiment, synthesized the polycrystalline powders, and successfully deposited the films. B. M. solved the crystal structure of the materials. B. M. and A. N. S. performed the structure refinements. M. E. C. helped with synthesis, FT-IR, Raman and NMR analysis. N. B. and D. C. L. helped with data interpretation, text and funding.

Data availability

Crystallographic data for $(Az)_3Bi_2I_9$ has been deposited at the CCDC crystallographic database under 2333118.† Crystallographic data for $(Az)_3Bi_2Br_9$ has been deposited at the CCDC crystallographic database under 2333116.† Crystallographic data for $(Az)_3Bi_2Cl_9$ has been deposited at the CCDC crystallographic database under 2333115.† No primary research results, software or code have been included.

Conflicts of interest

There are no conflicts to declare.

Acknowledgements

A. N. S acknowledges the support of the project CICECO-Aveiro Institute of Materials, UIDB/50011/2020, UIDP/50011/2020 & LA/P/0006/2020, financed by national funds through the FCT/MEC (PID-DAC). D. C. L., N. B., and Y. U. J acknowledge funding through the German Science Foundation (Deutsche Forschungsgemeinschaft, DFG) under project number 424708448. Fruitful discussions with Vladimir V. Shvartsman are highly acknowledged. Felix Niemeyer is acknowledged for his NMR measurements. Matthias Epple and Ivanna Kostina are acknowledged for the help of FT-IR measurement. Ulrich Hagemann is acknowledged for the help of Raman spectroscopy.

Notes and references

1 A. Kojima, K. Teshima, Y. Shirai and T. Miyasaka, Organometal halide perovskites as visible-light sensitizers for photovoltaic cells, *J. Am. Chem. Soc.*, 2009, **131**(17), 6050–6051.
2 J. H. Im, C. R. Lee, J. W. Lee, S. W. Park and N. G. Park, 6.5% efficient perovskite quantum-dot-sensitized solar cell, *Nanoscale*, 2011, **3**, 4088–4093.
3 M. M. Lee, J. Teuscher, T. Miyasaka, T. N. Murakami and H. J. Snaith, Efficient hybrid solar cells based on meso-superstructured organometal halide perovskites, *Science*, 2012, **338**, 643–647.
4 National Renewable Energy Laboratory, Best research-cell efficiency chart, accessed, 01, 2024, https://www.nrel.gov/pv/assets/images/efficiency-chart.png.
5 S. D. Stranks, G. E. Eperon, G. Grancini, C. Menelaou, M. J. P. Alcocer, T. Leijtens, L. M. Herz, A. Petrozza and H. J. Snaith, Electron-hole diffusion lengths exceeding 1 micrometer in an organometal trihalide perovskite absorber, *Science*, 2013, **342**(6156), 341–344.
6 M. Liu, M. B. Johnston and H. J. Snaith, Efficient planar heterojunction perovskite solar cells by vapour deposition, *Nature*, 2013, **501**, 395–398.
7 A. K. Jena, A. Kulkarni and T. Miyasaka, Halide perovskite photovoltaics: background, status, and future prospects, *Chem. Rev.*, 2019, **119**, 3036–3103.
8 L. N. Quan, B. P. Rand, R. H. Friend, S. G. Mhaisalkar, T. Lee and E. H. Sargent, Perovskites for next-generation optical sources, *Chem. Rev.*, 2019, **119**, 7444–7477.
9 M. Lyu, J. Yun, M. Cai, Y. Jiao, P. V. Bernhardt, M. Zhang, Q. Wang, A. Du, H. Wang, G. Liu and L. Wang, Organic–inorganic bismuth (III)-based material: A lead-free, air-stable and solution-processable light-absorber beyond organolead perovskites, *Nano Res.*, 2016, **9**(3), 692–702.
10 N. Cates and M. Bernechea, Research Update: Bismuth based materials for photovoltaics, *APL Mater.*, 2018, **6**, 084503.
11 S. Attique, N. Ali, S. Ali, R. Khatoon, N. Li, A. Khesro, S. Rauf, S. Yang and H. Wu, A potential checkmate to lead: bismuth in organometal halide perovskites, structure, properties, and applications, *Adv. Sci.*, 2020, **7**, 1903143.
12 X. Chen, M. Jia, W. Xu, G. Pan, J. Zhu, Y. Tian, D. Wu, X. Li and Z. Shi, Recent progress and challenges of bismuth-based halide perovskites for emerging optoelectronic applications, *Adv. Opt. Mater.*, 2023, **11**, 2202153.
13 K. M. McCall, C. C. Stoumpos, S. S. Kostina, M. G. Kanatzidis and B. W. Wessels, Strong Electron–Phonon Coupling and Self-Trapped Excitons in the Defect Halide Perovskites $A_3M_2I_9$ (A = Cs, Rb; M = Bi, Sb), *Chem. Mater.*, 2017, **29**, 4129–4145.
14 Y. E. Ajjouri, V. S. Chirvony, N. Vassilyeva, M. Sessolo, F. Palazon and H. J. Bolink, Low-dimensional non-toxic $A_3Bi_2X_9$ compounds synthesized by a dry mechanochemical route with tunable visible photoluminescence at room temperature, *J. Mater. Chem. C*, 2019, **7**, 6236–6240.
15 B. Chabot and E. Parthé, $Cs_3Sb_2I_9$ and $Cs_3Bi_2I_9$ with the hexagonal $Cs_3Cr_2Cl_9$ structure type, *Acta Crystallogr.*, 1978, **B34**, 645–648.

16 V. I. Sidey, Y. V. Voroshilov, S. V. Kun and E. Y. Peresh, Crystal growth and X-ray structure determination of $Rb_3Bi_2I_9$, *J. Alloys Compd.*, 2000, **296**, 53–58.

17 A. J. Lehner, D. H. Fabini, H. A. Evans, C. Hebert, S. R. Smock, J. Hu, H. Wang, J. W. Zwanziger, M. L. Chabinyc and R. Seshadri, Crystal and Electronic Structures of Complex Bismuth Iodides $A_3Bi_2I_9$ (A = K, Rb, Cs) Related to Perovskite: Aiding the Rational Design of Photovoltaics, *Chem. Mater.*, 2015, **27**, 7137–7148.

18 J. K. Pious, M. L. Lekshmi, C. Muthu, R. B. Rakhi and C. Vijayakumar, Zero-dimensional methylammonium bismuth iodide-based lead-free perovskite capacitor, *ACS Omega*, 2017, **2**, 5798–5802.

19 K. Hong, J. Kim, L. Debbichi, H. Kim and S. H. Im, Band Gap Engineering of $Cs_3Bi_2I_9$ Perovskites with Trivalent Atoms Using a Dual Metal Cation, *J. Phys. Chem. C*, 2017, **121**, 969–974.

20 B. Ghosh, S. Chakraborty, H. Wei, C. Guet, S. Li, S. Mhaisalkar and N. Mathews, Poor Photovoltaic Performance of $Cs_3Bi_2I_9$: An Insight through First-Principles Calculations, *J. Phys. Chem. C*, 2017, **121**, 17062–17067.

21 M. Shi, G. Li, W. Tian, S. Jin, X. Tao, Y. Jiang, E. A. Pidko, R. Li and C. Li, Understanding the effect of crystalline structural transformation for lead-free inorganic halide perovskites, *Adv. Mater.*, 2020, **32**, 2002137.

22 A. J. Lehner, D. H. Fabini, H. A. Evans, C. A. Hébert, S. R. Smock, J. Hu, H. Wang, J. W. Zwanziger, M. L. Chabinyc and R. Seshadri, Crystal and Electronic Structures of Complex Bismuth Iodides $A_3Bi_2I_9$ (A = K, Rb, Cs) Related to Perovskite: Aiding the Rational Design of Photovoltaics, *Chem. Mater.*, 2015, **27**, 7137–7148.

23 S. Sun, S. Tominaka, J. Lee, F. Xie, P. D. Bristowe and A. K. Cheetham, Synthesis, crystal structure, and properties of a perovskite-related bismuth phase, $(NH_4)_3Bi_2I_9$, *APL Mater.*, 2016, **4**, 031101.

24 K. M. McCall, C. C. Stoumpos, O. Y. Kontsevoi, G. C. B. Alexander, B. W. Wessels and M. G. Kanatzidis, From 0D $Cs_3Bi_2I_9$ to 2D $Cs_3Bi_2I_6Cl_3$: Dimensional Expansion Induces a Direct Band Gap but Enhances Electron–Phonon Coupling, *Chem. Mater.*, 2019, **31**, 2644–2650.

25 K. Ahmad, P. Kumar, H. Kim and S. M. Mobin, Optoelectronic and Photovoltaic Properties of $(NH_4)_3Bi_2I_9$: A Perovskite-like Energy Material for Pb-free Perovskite Solar Cells, *ChemNanoMat*, 2022, **8**, e20220006.

26 M. Pazoki, M. B. Johansson, H. Zhu, P. Broqvist, T. Edvinsson, G. Boschloo and E. M. J. Johansson, Bismuth iodide perovskite materials for solar cell applications: electronic structure, optical transitions, and directional charge transport, *J. Phys. Chem. C*, 2016, **120**(51), 29039–29046.

27 F. Ünlü, A. Kulkarni, K. Lê, C. Bohr, A. Bliesener, S. D. Öz, A. K. Jena, Y. Ando, T. Miyasaka, T. Kirchartz and S. Mathur, Single- or double A-site cations in $A_3Bi_2I_9$ bismuth perovskites: What is the suitable choice?, *J. Mater. Res.*, 2021, **36**, 1794–1804.

28 G. Kieslich, S. Sun and A. K. Cheetham, Solid-state principles applied to organic–inorganic perovskites: new tricks for an old dog, *Chem. Sci.*, 2014, **5**, 4712–4715.

29 G. Kieslich, S. Sun and A. K. Cheetham, An extended tolerance factor approach for organic–inorganic perovskites, *Chem. Sci.*, 2015, **6**, 3430–3433.

30 M. Mączka, T. A. da Silva, W. Paraguassu, M. Ptak and K. Hermanowicz, Raman and IR Studies of Pressure- and Temperature-Induced Phase Transitions in $[(CH_2)_3NH_2]$-$[Zn(HCOO)_3]$, *Inorg. Chem.*, 2014, **53**, 12650–12657.

31 T. Asaji, Y. Ito, H. Fujimori and B. Zhou, Ring-Puckering Motion of Azetidinium Cations in a Metal–Organic Perovskite $[(CH_2)_3NH_2][M(HCOO)_3]$ (M = Zn, Mg)—A Thermal and 1H NMR Relaxation Study, *J. Phys. Chem. C*, 2019, **123**, 4291–4298.

32 M. Rok, M. Moskwa, J. Hetmańczyk, Ł. Hetmańczyk and G. Bator, Switchable dielectric constant, structural and vibrational studies of double perovskite organic–inorganic hybrids: $(azetidinium)_2[KCr(CN)_6]$ and $(azetidinium)_2[KFe(CN)_6]$, *CrystEngComm*, 2022, **24**, 4932–4939.

33 S. R. Pering, W. Deng, J. R. Troughton, P. S. Kubiak, D. Ghosh, R. G. Niemann, F. Brivio, F. E. Jeffrey, A. B. Walker, M. S. Islam, T. M. Watson, P. R. Raithby, A. L. Johnson, S. E. Lewis and P. J. Cameron, Azetidinium lead iodide for perovskite solar cells, *J. Mater. Chem. A*, 2017, **5**, 20658–20665.

34 R. Panetta, G. Righini, M. Colapietro, L. Barba, D. Tedeschi, A. Polimeni, A. Ciccioli and A. Latini, Azetidinium lead iodide: synthesis, structural and physico-chemical characterization, *J. Mater. Chem. A*, 2018, **6**, 10135–10148.

35 Y. U. Jin, B. Marler, A. D. Karabanov, K. Winkler, I. C. J. Yap, A. Dubey, L. Spee, M. E. Castillo, F. Muckel, A. N. Salak, N. Benson and D. C. Lupascu, Lead-free organic–inorganic azetidinium alternating metal cation bromide:$[(CH_2)_3NH_2]_2AgBiBr_6$, a perovskite-related absorber, *RSC Adv.*, 2023, **13**, 36079–36087.

36 A. Altomare, C. Cuocci, C. Giacovazzo, A. Moliterni, R. Rizzi, N. Corriero and A. Falcicchio, EXPO2013: a kit of tools for phasing crystal structures from powder data, *J. Appl. Cryst.*, 2013, **46**, 1231–1235.

37 R. Hoye, R. E. Brandt, A. Osherov, V. Stevanovic, S. D. Stranks, M. W. B. Wilson, H. Kim, A. J. Akey, R. C. Kurchin, J. R. Poindexter, E. N. Wang, M. G. Bawendi, V. Bulovic and T. Buonassisi, Methylammonium bismuth iodide as a lead-free, stable hybrid organic–inorganic solar absorber, *Chem. – Eur. J.*, 2016, **22**, 2605–2610.

38 P. Szklarz, A. Pietraszko, R. Jakubas, G. Bator, P. Zielinski and M. Gałazka, Structure, phase transitions and molecular dynamics of $[C(NH_2)_3]_3[M_2I_9]$, M= Sb, Bi, *J. Phys.: Condens. Matter*, 2008, **20**, 255221.

39 H. Günter, G. Schrem and H. Oberhammer, The gas-phase structure of azetidine: Microwave spectroscopy, and electron diffraction and normal coordinate analysis, *J. Mol. Spectrosc.*, 1984, **104**, 152–164.

40 P. H. Nielsen and M. Gajhede, Reassignment of the fundamental vibrations of azetidine from ab initio calculations, *J. Phys. Org. Chem.*, 1989, **2**, 183–186.

41 H. G. O. Becker, G. Domschke, E. Fanghänel, M. Fischer, K. Gewald, R. Mayer, D. Pavel, H. Schmidt and K. Schwetlick, *Organikum*, 1990, **A.3.5**, 86–88.

42 A. Nila, M. Baibarac, A. Matea, R. Mitran and I. Baltog, Exciton–phonon interactions in the $Cs_3Bi_2I_9$ crystal structure revealed by Raman spectroscopic studies, *Phys. Status Solidi B*, 2017, **254**(No. 4), 1552805.

43 G. M. Paternò, N. Mishra, A. J. Barker, Z. Dang, G. Lanzani, L. Manna and A. Petrozza, Broadband Defects Emission and Enhanced Ligand Raman Scattering in 0D $Cs_3Bi_2I_9$ Colloidal Nanocrystals, *Adv. Funct. Mater.*, 2019, **29**, 1805299.

44 A. Miniewicz, R. Jakubas, C. Ecolivet and A. Girard, Raman scattering in ferroelectric $(CH_3NH_3)_3Bi_2Br_9$ single crystals, *J. Raman Spectrosc.*, 1994, **25**, 371–375.

45 L. El-Adel, A. Ouasri, A. Rhandour and L. Hajji, Raman-Infrared spectroscopy, thermal behaviour, dielectric, and UV-fluorescence studies of $[C_6H_5NH_3]_3BiCl_6{\cdot}3H_2O$, *Solid State Commun.*, 2021, **340**, 114541.

46 A. Ouasri, F. Lambarki, R. Fakherddine, A. Aatiq and A. Rhandour, Structural characterisation, BFDH morphology, DSC, infrared and Raman studies of the disordered tetramethylammonium nonachlorodibismuthate $[(CH_3)_4N]_3$-Bi_2Cl_9, *Polyhedron*, 2024, **251**, 116875.

47 P. Kubelka and F. Munk, An article on optics of paint layers, *Z. Tech. Phys.*, 1931, **12**, 593–601.

48 P. Makuła, M. Pacia and W. Macyk, How to correctly determine the band gap energy of modified semiconductor photocatalysts based on UV-vis spectra, *J. Phys. Chem. Lett.*, 2018, **9**, 6814–6817.

49 F. Ünlü, M. Deo, S. Mathur, T. Kirchartz and A. Kulkarni, Bismuth-based halide perovskite and perovskite-inspired light absorbing materials for photovoltaics, *J. Phys. D: Appl. Phys.*, 2022, **55**, 113002.

50 X. Chen, Y. Myung, A. Thind, Z. Gao, B. Yin, M. Shen, S. B. Cho, P. Cheng, B. Sadtler, R. Mishra and P. Banerjee, Atmospheric pressure chemical vapor deposition of methylammonium bismuth iodide thin films, *J. Mater. Chem. A*, 2017, **5**, 24728.

51 B. Park, B. Philippe, X. Zhang, H. Rensmo, G. Boschloo and E. M. J. Johansson, Bismuth Based Hybrid Perovskites $A_3Bi_2I_9$ (A: Methylammonium or Cesium) for Solar Cell Application, *Adv. Mater.*, 2015, **27**, 6806–6813.

52 C. Wu, Q. Zhang, G. Liu, Z. Zhang, D. Wang, B. Qu, Z. Chen and L. Xiao, From Pb to Bi: A promising family of Pb-free optoelectronic materials and devices, *Adv. Energy Mater.*, 2020, **10**, 1902496.

53 G. M. Paternò, N. Mishra, A. J. Barker, Z. Dang, G. Lanzani, L. Manna and A. Petrozza, Broadband Defects Emission and Enhanced Ligand Raman Scattering in 0D $C_s3Bi_2I_9$ Colloidal Nanocrystals, *Adv. Funct. Mater.*, 2019, **29**, 1805299.

54 T. Kawai, A. Ishii, T. Kitamura, S. Shimanuki, M. Iwata and Y. Ishibashi, Optical Absorption in Band-Edge Region of $(CH_3NH_3)_3Bi_2I_9$ Single Crystals, *J. Phys. Soc. Jpn.*, 1996, **65**(5), 1464–1468.

55 J. Klein, L. Kampermann, B. Mockenhaupt, M. Behrens, J. Strunk and G. Bacher, Limitations of the Tauc plot method, *Adv. Funct. Mater.*, 2023, **33**, 2304523.

56 D. Han, H. Shi, W. Ming, C. Zhou, B. Ma, B. Saparov, Y. Ma, S. Chen and M. Du, Unraveling luminescence mechanisms in zero-dimensional halide perovskites, *J. Mater. Chem. C*, 2018, **6**, 6398–6405.

57 I. Rörich, Q. Niu, B. van der Zee, E. del Pino Rosendo, N. I. Crăciun, C. Ramanan and P. W. M. Blom, Exciton Quenching due to Hole Trap Formation in Aged Polymer Light-Emitting Diodes, *Adv. Electron. Mater.*, 2020, **6**, 1700643.

58 S. Athanasopoulos, E. Hennebicq, D. Beljonne and A. B. Walker, Trap Limited Exciton Transport in Conjugated Polymers, *J. Phys. Chem. C*, 2008, **112**, 11532–11538.